LA-UR-19-20174
Approved for public release; distribution is unlimited.

Title: PBX 9502 Failure Diameter: Addendum

Author(s): Menikoff, Ralph

Intended for: Report

Issued: 2019-11-21 (rev.1)

PBX 9502 Failure Diameter: Addendum

Ralph Menikoff

November 18, 2019

Abstract

In previous reports, the SURFplus reactive burn model was used to study a propagating detonation wave for PBX 9502 in an unconfined rate stick just above the failure diameter. Simulations showed that the sonic boundary condition at the HE interface leads to a boundary layer. Here we provide additional details on the steady-state flow with emphasis on the boundary layer. This confirms the previous conclusion that within the boundary layer the lead shock, which initiates the hot-spot reaction, is largely supported by transverse energy flow in the reaction zone from the interior towards the boundary. Consequently, the reactive wave along a boundary layer streamline does not correspond to a 1-D detonation wave in the sense of detonation shock dynamics; *i.e.*, the lead shock which initiates the reaction is not driven by the reaction energy along the streamline.

1 Introduction

The SURFplus reactive burn model [Menikoff and Shaw, 2012] has a fast hot-spot reaction rate and a slow carbon clustering reaction rate. The fast rate dominates shock initiation and the slow rate is needed to fit the curvature effect. In addition, the model rate has a parameter to account for the effect of a pressure gradient behind the lead shock. This is needed to fit the failure diameter.

Propagating detonation waves are characterized by the curvature effect (detonation speed as a function of local front curvature) and the failure diameter (minimum diameter of an unconfined rate stick that can support a detonation wave). Previously, it was shown that the SURFplus reactive burn model can be calibrated for PBX 9502 to fit both these properties [Menikoff, 2017a]. In addition, it was noted that the sonic boundary condition led to a boundary layer in which the lead shock pressure varied rapidly as the HE boundary is approached [Menikoff, 2017a, fig 8] & [Menikoff, 2017c, fig 3], and the failure mechanism below the failure diameter was discussed.

Subsequently, the rate was recalibrated for hot and cold as well as ambient PBX 9502 [Menikoff, 2017b]. For the ambient case there was a slight adjustment to the Pop plot used to calibrate the shock initiation regime. A follow up paper reported on a resolution study. With sufficiently fine resolution it was found that the simulated shape of the detonation front closely approaches the experimentally measured shape [Menikoff, 2017c, fig 3].

Here we supply additional details on the steady-state flow in the layer adjacent to the HE boundary. This supports the previous conclusion that the lead shock within the boundary layer is largely supported by transverse energy flow in the reaction zone from the interior towards the boundary. Consequently, the reactive wave along a boundary layer streamline does not correspond to a 1-D detonation wave in the sense of detonation shock dynamics (DSD) [Bdzil and Stewart, 2007]; *i.e.*, the lead shock that initiates the reaction is not driven by the reaction energy along a boundary layer streamline.

The transverse reaction zone flow is related to the extended DSD theory [Aslam et al., 1998], which is needed to explain experimental measurements that show for large front curvature (κ) the local detonation speed depends on the rate stick diameter [Hill et al., 1998] rather than a local properties $D_n(\kappa)$ as assumed in the first order theory. It also raises the question of the DSD boundary condition when the HE is weakly confined.

The transverse flow in the reaction zone can also explain the failure to propagate a detonation wave below the failure diameter. Starting with an overdriven detonation wave, the energy flow to the outer radii is too much of a loss and leads to a failure wave propagating inward from the

boundary. When the failure wave reaches the axis, the detonation wave completely fails over the entire lead shock front; see [Menikoff, 2017a].

2 Simulations

The simulations described here use the same burn model and setup as in the resolution study for the very-fine case in Menikoff [2017c]; 5 mm radius unconfined rate stick with a 4 μm cell size in the reaction zone (256 cells per mm). Profiles of the pressure and reaction progress variable shown in [Menikoff, 2017c, fig 2] along the axis and near the HE boundary indicate that the reaction zone is fairly well resolved.

The model formulation and parameters of the SURFplus reactive burn model for ambient PBX 9502 are given in [Menikoff, 2017b, appendices and table 2]. The setup corresponds to that shown in [Menikoff, 2017a, fig 2]. The rate stick of interest is initiated with a detonation wave from a wider rate stick. The detonation wave runs long enough (5 diameters) to reach steady state as indicated by probe points (numerical timing pins) on the axis that show a constant detonation speed [Menikoff, 2017c, fig 1] and Eulerian tracer particles that show the same pressure time histories at different axial positions [Menikoff, 2017a, fig 5].

The probe points give a steady-state axial detonation speed of 7.475 km/s compared to the CJ detonation speed of 7.782 km/s. From the reactants EOS, the shock pressure on axis is 38.7 GPa compared to the planar von Neumann spike pressure of 43.6 GPa.

In addition, for the current simulation, near the end of the rate stick, Lagrangian tracer particles are distributed along a radius at a constant axial position to get reaction-zone time histories of key reaction variables. The tracer particle data are post processed utilizing steady-state relations to shift the axial positions of the tracers such that $y(r)$ at shock arrival corresponds to the shape of the detonation front at a fixed time. Also, the axial velocity is shifted to correspond to the rest frame of the detonation front. Then the streamlines $\big(r(t), y(t)\big)$ and the stream distance behind the front s are computed by integrating the velocity for each tracer.

3 Numerical results

Streamlines for the steady-state detonation are shown in fig. 1. The sonic curve is also shown on the plot. The flow behind the sonic curve does not affect the reaction region between the shock front and the sonic curve. As previous noted, the flow is sonic at the HE boundary. Based

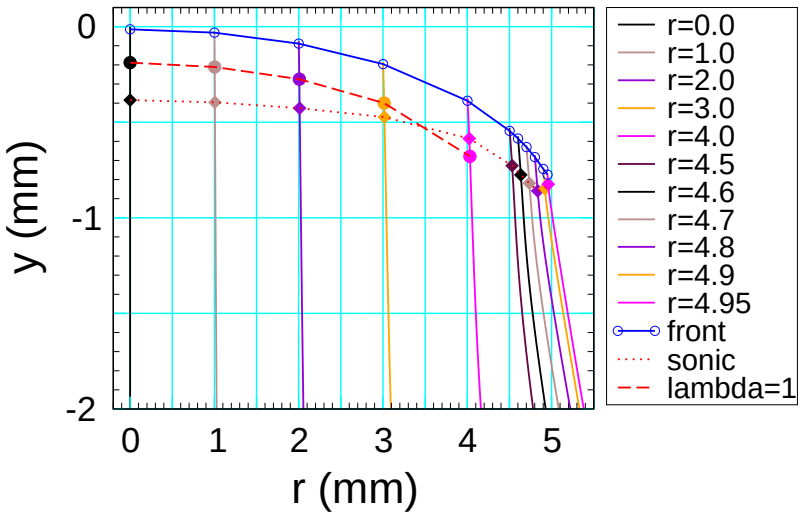

Figure 1: Streamlines in steady-state frame starting at the detonation front for initial radii listed in the legend. Diamonds and dotted red line correspond to the sonic point with respect to the detonation front. Circles and dashed red line correspond to the completion of the fast hot spot rate. Note that the axial scale (y) is stretched relative to the radial scale (r).

on the shock polar at the axial detonation speed for the reactants EOS, the sonic pressure is about 15 GPa.

The last tracer particle is 0.05 mm from the HE boundary. Since the air pressure surrounding the HE is insignificant, there is a rapid variation of the pressure as the HE boundary is approached. Higher resolution would be needed to get accurate tracer particle data closer to the boundary.

The pressure along the shock front and along streamlines is shown in fig. 2. The front pressure varies from 38 GPa at the axis to 15 GPa at the boundary. The calibrated rate [see Menikoff, 2017b, fig 2], which is a function of the lead shock pressure, varies by about a factor of 40. We note that the sonic pressure is about the high end of Pop plot data. Hence, the rate at the sonic pressure is determined by shock initiation experiments. Away from the boundary, the pressure gradient along a streamline behind the shock front is supported by the energy release from the reaction.

The reaction progress variables along streamlines are shown in fig. 3. Up to a radius of $r = 3$ mm, the fast reaction completes and the sonic point is within the region in which the slow reaction is occurring. For the outer radii $r > 4.5$ mm, the sonic point occurs before the fast reaction completes and with a very small amount of the slow reaction. Close to the boundary,

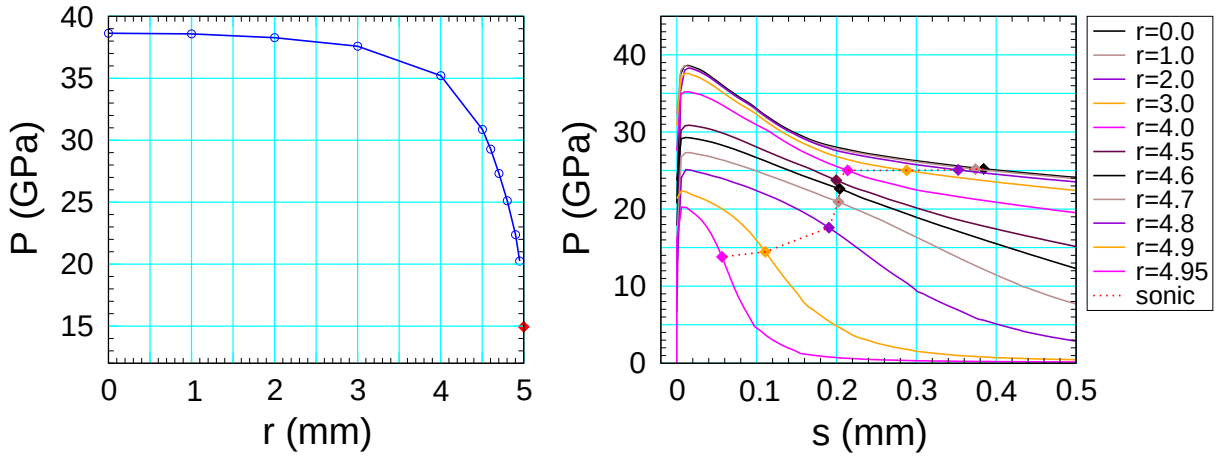

Figure 2: Pressure along shock front as function of radius and pressure along streamlines. For shock front, blue circles denote tracer particle positions and red diamond denotes sonic point on the shock polar.

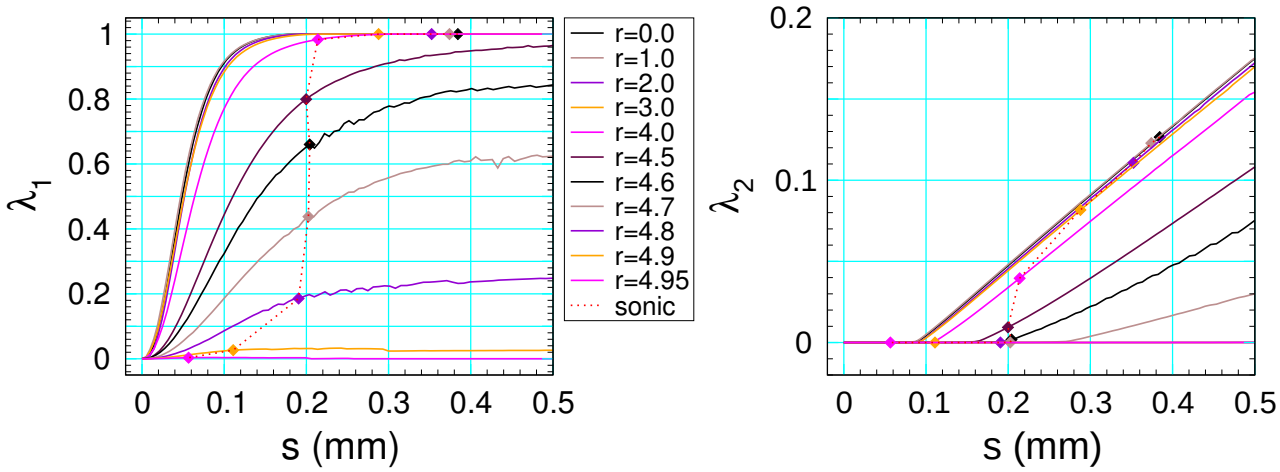

Figure 3: Reaction progress variables as function of stream variable in steady-state frame; λ_1 and λ_2 for fast (hot spot) reaction and slow (carbon clustering) reaction, respectively. Diamond symbols indicates sonic point with respect to the detonation front.

the amount of the fast reaction along the streamline before the sonic point is too low to support the lead shock.

The rapid change in shock pressure near the boundary gives rise to a significant pressure gradient transverse to the streamlines. This results in a radial flow of energy. The equation for

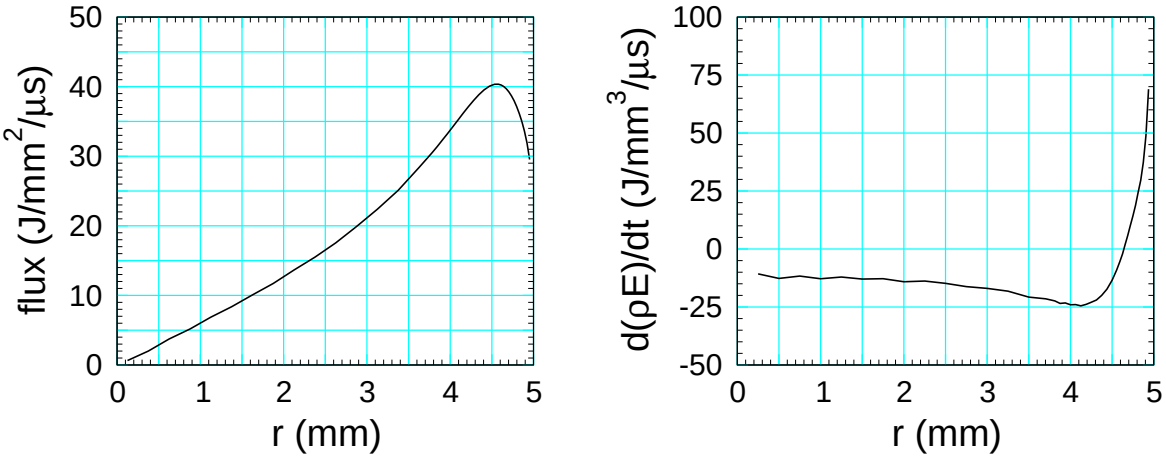

Figure 4: Radial component of the energy flux along shock front and radial energy transfer in the Lab frame. $\mathsf{d}(\rho\, E)/\mathsf{d}t < 0$ represents an energy loss from the radial flux.

conservation of energy can be expressed as

$$\frac{\partial}{\partial t}\Big[\rho\, E\Big] = -\nabla \cdot \Big[\rho\, \vec{u}\big(E + P\, V\big)\Big]\ , \tag{1}$$

where $E = e + \frac{1}{2}|\vec{u}|^2$ is the total specific energy. The radial component of the energy flux is $\text{flux}_r = \rho\, u_r(E + P\, V)$ where $u_r = \hat{r} \cdot \vec{u}$ is the radial component of the particle velocity and the contribution to the left hand side, *i.e.*, radial energy flow, is $-r^{-1}\partial_r(r \cdot \text{flux}_r)$.

At the front, the radial energy flux can be calculated using the front pressure from the simulation, $P(r)$, and the shock Hugoniot for the reactants EOS, which determines the complete state behind the front. In the Lab frame, the energy flux and radial energy is shown in fig. 4. We note that $\mathsf{d}(\rho\, E)/\mathsf{d}t < 0$ except for a thin layer adjacent to the boundary. The energy loss peaks at a radius corresponding to the start of the boundary layer. The positive radial energy flow is supporting the shock in the vicinity of the boundary. The energy flow at the boundary is significant compared to the shock energy at the sonic point of $\rho E = 5.3\,\text{J/mm}^3$.

Physically, a shock is supported by the upstream flow. We note that upstream depends on the frame of reference. In the rest frame of the detonation front, the mass flux ($\rho_0 u_s$) and the Bernoulli function ($E + PV$) are constant across the shock front. In this frame, the lead shock is supported by the kinetic energy in the flow ahead of the shock, *i.e.*, the low pressure side of the shock front. In the Lab frame, upstream corresponds to the high pressure side of the front. For the radial flow supporting the lead shock in the boundary layer, it is important to use the flux in the Lab frame.

3.1 Local frame normal to front

DSD theory [Bdzil and Stewart, 2007] is based on several approximations which reduce the flow in the reaction zone to a series of 1-D problems along streamlines. It is instructive to compare the numerical solution for a steady detonation in an unconfined rate stick with the DSD approximation.

Starting in the rest frame of detonation front (incoming velocity in the negative axial direction with the axial detonation speed) the leading order DSD theory can be expressed in terms of the following steps:

1. For a point on the detonation front, rotate to a local frame in which one coordinate is normal to the detonation front.

2. Make a Galilean transformation such that the tangential component of the incoming streamline is zero. Consequently, the flow both ahead and behind the shock front is normal to the front.

3. Consider a stream tube formed by neighboring streamlines. Assume that the streamlines in the reaction zone are straight lines. This is tantamount to neglecting transverse gradients. By definition, the component of velocity perpendicular to a streamline is zero. Consequently, there is no advection or PV energy transfer into or out of the stream tube. The steady flow in the stream tube corresponds to the ODEs for reactive duct flow. Furthermore, it can be shown from the deflection of the streamlines through the shock that the cross sectional area of the duct is given by $\partial_s A/A = \kappa$, the mean curvature of the detonation front. For the DSD theory, $D_n(\kappa)$ is taken as the solution of these equation which is non-singular at the sonic point.

4. Use the inverse transforms of the first 2 steps to map the solution of the duct flow equations to the streamlines in the steady frame.

The key approximation is that the transverse pressure gradient can be neglected and the streamlines are straight lines. This implies that the curvature is slowly varying along the detonation front. For a cylindrically or spherically diverging detonation, we note that the front curvature is constant and the transverse gradients are zero. However, in this case, κ is time dependent and one needs to assume that the reaction zone is quasi steady; *i.e.*, the change in the front radius over the reaction time is small, which is equivalent to $\kappa \cdot$ (reaction-zone width) is small.

It is important to note that the streamlines depend on the reference frame. From the tracer particle data, the streamlines in the local frame normal to the front can be computed. Reversing

the coordinate transformation but not the Galilean transformation, yields a coordinate system in which the image of a constant streamline coordinate s is approximately parallel to the shock front. From the numerical solution, the normal frame streamlines are shown in fig. 5. We note that the angles between the front and the streamlines are distorted since the r and y scales on the plot are not 1 to 1.

Profiles along the transformed tracer particle streamlines of the pressure and stream angle with the axis are shown in fig. 6 and fig. 7, respectively. We observe that up to an initial streamline radius of 3 mm, there is small difference in the profiles $P(s)$ and the stream angle is nearly constant. Thus, for these streamlines the DSD approximation is valid.

In the boundary layer, streamlines with initial radius greater than 4.5 mm, the pressure profiles considerably decrease as the radius increases. Hence the transverse pressure gradient within the reaction is significant, and the stream angle is not constant. For the last 0.2 mm from the HE interface, the streamline angle varies by a large amount due to the centered rarefaction following the lead shock at the HE boundary. Consequently, the 1-D detonation profile ODEs used by the DSD theory are not an accurate representation of the flow in the boundary layer. In fact the ODEs for rate model only have a solution for $D_n(\kappa)$ over a limited domain in κ which does not include the the large values of κ in the boundary layer; see [Menikoff, 2017b, fig 6 and 7].

Finally, in the local normal frame, the state behind the shock is alway subsonic. This is not compatible with the sonic condition at the unconfined boundary leading to the centered rarefaction at the boundary. Thus, there is an issue with the DSD boundary condition for the weak confinement case.

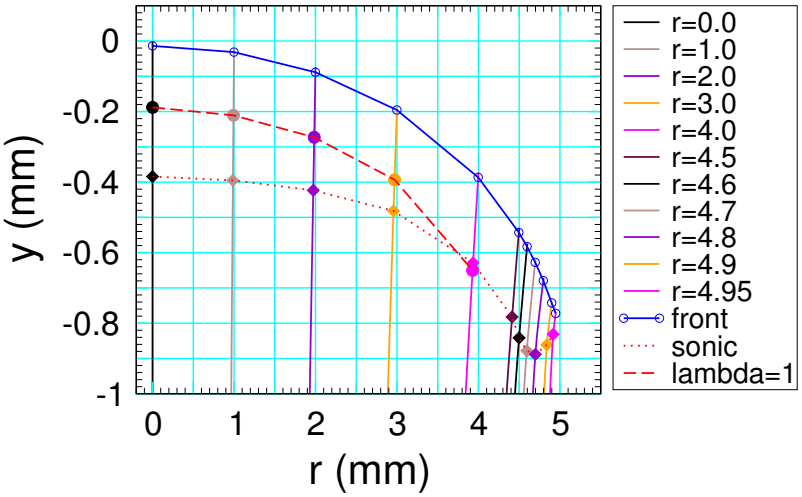

Figure 5: Streamlines in local frame normal to the detonation front for initial radii listed in the legend. Diamonds and dotted red line correspond to the sonic point with respect to the detonation front. Circles and dashed red line correspond to the completion of the fast hot-spot rate. Note that the axial scale (y) is stretched relative to the radial scale (r).

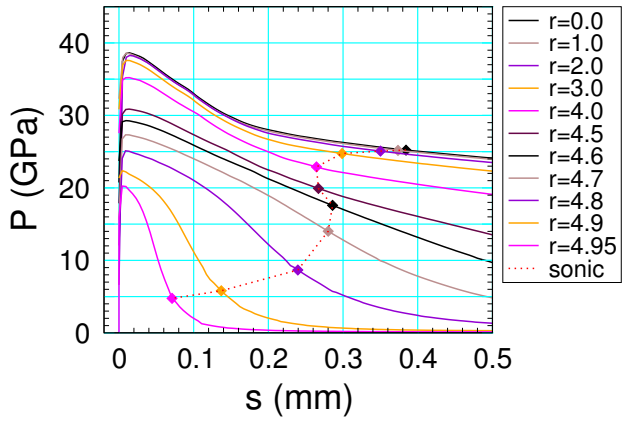

Figure 6: Pressure along local normal frame stream lines for initial radii listed in legend. Symbols indicate sonic point.

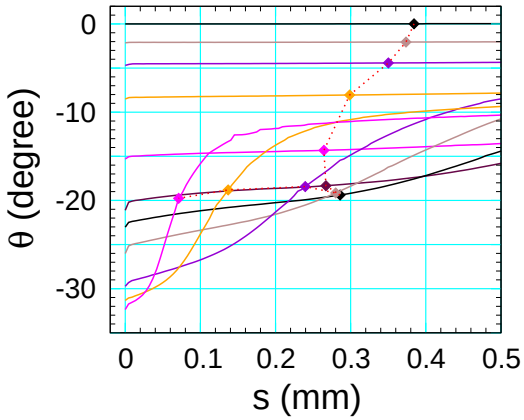

Figure 7: Streamline angle along local normal frame streamlines; $\theta = \tan^{-1}(u_x/u_y)$.

3.2 Carbon cluster growth

Small angle X-ray scattering experiments have been used to investigate the growth of carbon cluster behind the detonation front of a PBX 9502 detonation wave in an unconfined rate stick [Watkins et al., 2017]. For the analysis of the average cluster size, the authors had to account for the detonation front curvature. In addition, they conjectured that a minimum temperature of about 2000 K is needed for the collision of two carbon clusters to result in their sticking together and the atoms redistribute to form a larger spherical clusters.

The experimental measurement of average carbon cluster radius at a given time is a volume weighted average over the rate stick radius of the response function for the cluster size as a function of radius. The carbon cluster reaction progress variable and the temperature along streamlines are shown in fig. 8 as a function of time behind the detonation front on the axis.

For the SURFplus model, the radius of carbon cluster is proportional to $[1+(N_{ratio}-1)\lambda_2]^{1/3}$, where N_{ratio} is the ratio of the final number to the initial number (after hot-spot reaction) of carbon atoms in a cluster; see [Menikoff and Shaw, 2012]. With $N_{ratio} = 50$ from the PBX 9502 calibration [Menikoff, 2017b], the cluster radius as a function of λ_2 is shown in fig. 9.

We note that for $r > 4.6\,\text{mm}$, which corresponds to the boundary layer, the temperature would be below the estimated cutoff for carbon clusters to grow, and would not contribute to the measurement. The cutoff occurs after the sonic point. Hence it would not affect either the shape of detonation front or the detonation speed. However, for some applications it could affect the energy release. The temperature cutoff on the carbon cluster rate is not in the current formulation of the SURFplus model.

3.3 Weakly confined case

Another simulation was run to show the importance of the sonic boundary condition. For the additional simulation the HE is surrounded by PMMA (polymethylmethacrylate) instead of air. Based on shock polar analysis, PMMA is weakly confining for PBX 9502; see for example [Short and Quirk, 2018, fig 4]. Hence, the sonic boundary condition applies.

The simulations show that the steady-state axial detonation speed of the rate stick is the same for both air and PMMA confinement. A comparison of streamlines, pressure along the streamline and streamline angle are shown in fig. 10. Up to the sonic point, it can be seen that the plots are the same. After the sonic point, the additional confinement from the higher PMMA density significantly reduces the outward expansion of the outer streamlines.

The result is that when the sonic boundary condition applies, the flow in the portion of the reaction zone between the detonation front and the sonic locus is independent of the confining

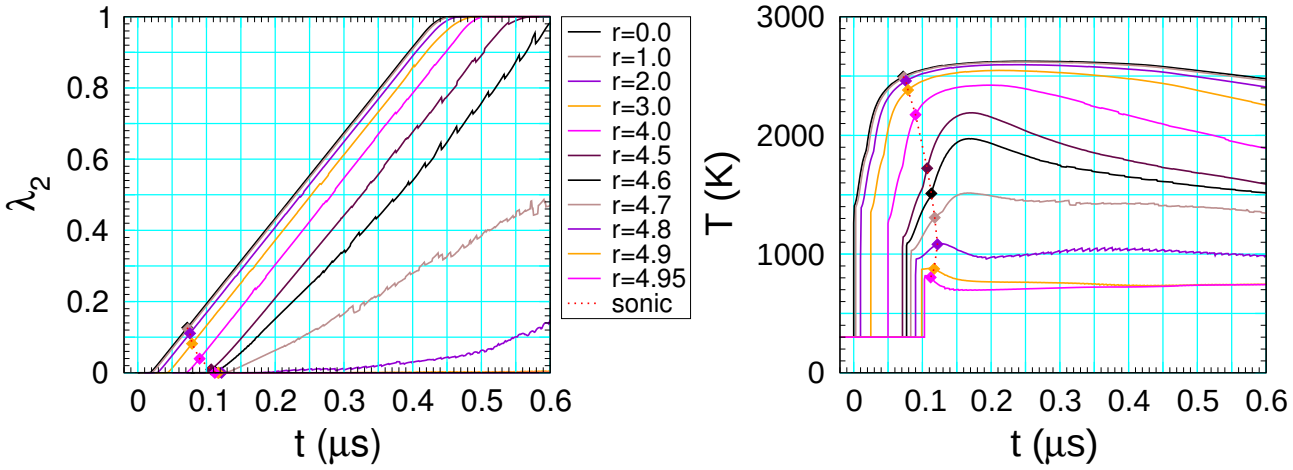

Figure 8: Time history along streamlines of second reaction progress variable and temperature. Diamond symbol indicates sonic point with respect to the detonation front. Offsets in shock arrival time are due to front curvature.

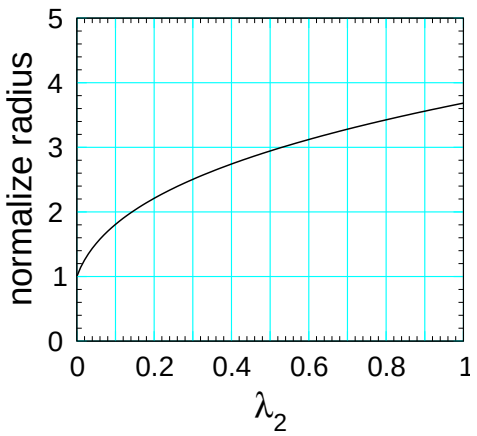

Figure 9: Normalized carbon cluster radius as function of reaction progress variable for $N_{ratio} = 50$.

material. This determines the detonation speed and the shape of the detonation frame. It also implies that the failure diameter is the same for all weakly confining materials.

We note that there is reaction behind the sonic locus. For PBX 9502, a significant amount of the carbon cluster energy is released behind the sonic locus; see fig. 3. This energy release is affected by the confinement. But the late energy release affects neither the detonation speed nor the shape of the detonation front.

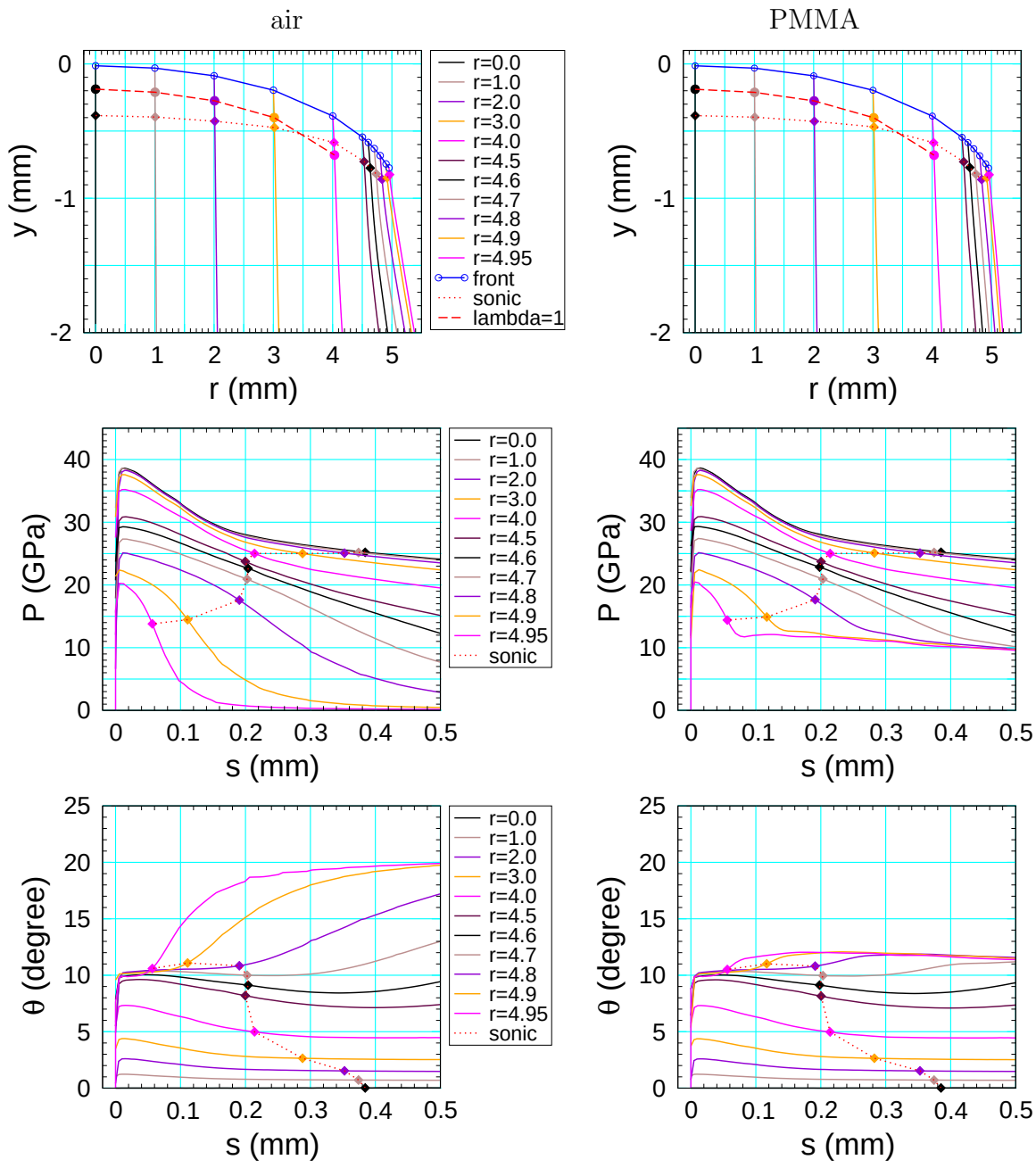

Figure 10: Comparison of rate stick confined by air and PMMA. In rest frame of detonation front, streamlines, pressure along streamlines and streamline angle are plotted. The initial streamline radii are listed in the legend. The diamond symbol indicates the sonic point.

4 Summary

For an unconfined rate stick, at the boundary, the lead shock is sonic. For PBX 9502, slightly above the failure diameter (10 mm) the shock pressure varies from about 38 GPa on axis to the sonic pressure of about 15 GPa at the HE boundary (5 mm radius). Most of the pressure drop occurs within a 0.5 mm boundary layer.

We also note that the sonic pressure is within the upper end of Pop plot data. Hence, the rate at the sonic pressure is determined by shock initiation data. From the SURF model calibration for ambient PBX 9502, the rate at the sonic pressure is a factor of 40 less than the rate on the axis; see [Menikoff, 2017b, fig 2]. Consequently, the full reaction zone width greatly increases towards the boundary. However, the reaction after the sonic locus does not affect the axial detonation speed.

An examination of the flow variables along Lagrangian streamlines in the rest frame of the lead shock shows that the amount of reaction at the sonic point rapidly decrease as the radius approaches the HE boundary. The lead shock in the boundary layer is supported by transverse energy flow in the reaction zone. Consequently, the reactive wave along a boundary layer streamline does not correspond to a 1-D detonation wave with the local front curvature in the sense of detonation shock dynamics; *i.e.*, the lead shock which initiates the reaction is not driven by the reaction energy along the streamline.

References

T. D. Aslam, J. B. Bdzil, and L. G. Hill. Extension to DSD theory: Analysis of PBX 9502 rate stick data. In *Proceeding of the Eleventh International Symposium on Detonation*, pages 21–29, 1998. 2

J. B. Bdzil and D. S. Stewart. The dynamics of detonation in explosive systems. *Annual Rev. Fluid Mech.*, 39:263–292, 2007. URL https://doi.org/10.1146/annurev.fluid.38.050304.092049. 2, 7

L. G. Hill, J. B. Bdzil, and T. D. Aslam. Front curvature rate stick measurements and detonation shock dynamics calibration for PBX 9502 over a wide temperature range. In *Proceeding of the Eleventh International Symposium on Detonation*, pages 1029–1037, 1998. 2

R. Menikoff. Failure diameter of PBX 9502: Simulations with the SURFplus model. Technical Report LA-UR-17-25300, Los Alamos National Lab., 2017a. URL https://doi.org/10.2172/1369155. 2, 3

R. Menikoff. SURFplus model calibration for PBX 9502. Technical Report LA-UR-17-31015, Los Alamos National Lab., 2017b. URL https://doi.org/10.2172/1412839. 2, 3, 4, 8, 10, 13

R. Menikoff. Failure diameter resolution study. Technical Report LA-UR-17-31380, Los Alamos National Lab., 2017c. URL https://doi.org/10.2172/1415358. 2, 3

R. Menikoff and M. S. Shaw. The SURF model and the curvature effect for PBX 9502. *Combustion Theory And Modelling*, pages 1140–1169, 2012. URL http://dx.doi.org/10.1080/13647830.2012.713994. 2, 10

M. Short and J. J. Quirk. High explosive detonation-confinement interactions. *Annual Review of Fluid Mechanics*, 50:215–242, 2018. URL https://doi.org/10.1146/annurev-fluid-122316-045011. 10

E. B. Watkins, B. Erik, K. A. Velizhanin, D. M. Dattelbaum, R. L. Gustavsen, T. D. Aslam, D. W. Podlesak, R. C. Huber, M. A. Firestone, B. S. Ringstrand, T. M. Willey, M. Bagge-Hansen, R. Hodgin, L. Lauderbach, T. van Buuren, N. Sinclair, P. A. Rigg, S. Seifert, and T. Gog. Evolution of carbon clusters in the detonation products of the triaminotrinitrobenzene (TATB)-based explosive PBX 9502. *Journal of Physical Chemistry C*, 121:23129–23140, 2017. URL https://doi.org/10.1021/acs.jpcc.7b05637. 10